






Application of a Change Detection Soil Moisture Retrieval Algorithm to Combined, Semiconcurrent Radiometer, and Radar Observations

Jeffrey D. Ouellette , Tanish Himani , Li Li , *Senior Member, IEEE*, Elizabeth M. Twarog ,
Andreas Colliander , David Goodrich , Chandra Holifield Collins, Michael Cosh,
and Jeffrey P. Walker , *Fellow, IEEE*

Abstract—This article extends the application of an existing change-detection-based, time-series soil moisture retrieval algorithm to nonconcurrent active and passive measurements from WindSat/AMSR2 and the Soil Moisture Active Passive radar, which was active from late April until mid-July of 2015. A time series of L-band radar backscatter observations was used to populate an underdetermined matrix equation whose optimal solution was derived via a bounded linear least squares estimator, and whose bounds were derived from a time series of radiometer-derived soil moisture estimates (taken by either WindSat or AMSR2). Surface soil moisture estimates are compared with in-situ measurement probes, which were treated as ground truth. Error statistics and time-series results for the validation sites are presented here and conclusions derived therefrom. The overall RMSE and unbiased RMSE for the retrieval algorithm, taken across all reference pixels considered in the study, were $0.070 \text{ m}^3/\text{m}^3$ and $0.067 \text{ m}^3/\text{m}^3$, respectively, when using WindSat to constrain the algorithm. When using AMSR2 to constrain the algorithm, the RMSE and unbiased RMSE were $0.093 \text{ m}^3/\text{m}^3$ and $0.090 \text{ m}^3/\text{m}^3$, respectively.

Index Terms—Change detection, data fusion, hydrology, radar, radiometer, remote sensing, retrieval algorithm, soil moisture, time series.

I. INTRODUCTION

HERE exists a long precedent for using radiometer brightness temperature for surface soil moisture (SSM) remote sensing, particularly at L-band frequencies [1], [2], [3], [4]. Radar backscatter has also become a popular tool for SSM retrieval algorithms, in part due to the comparatively higher spatial resolution that radar systems can achieve. This study expands on previous work in the domain of combined active/passive (radar/radiometer), approaches to retrieving SSM from vegetated surfaces using space-borne sensors [5]. In particular, this work demonstrates the utility in combining nonsimultaneous, frequency-diverse measurements to provide stable, accurate, high-resolution SSM data products.

In a previous study, it was shown that a radiometer-constrained radar change detection algorithm could be used to combine simultaneous time-series observations from an L-band radiometer and an L-band radar on-board the soil moisture active passive (SMAP) satellite to form accurate, high-resolution (3 km) SSM products [5] during the SMAP radar's operation from late April until mid-July of 2015. The strength of this algorithm, whose formulation is detailed in the following section, lies in its simplicity: the radar portion of the algorithm does not require any parameter/curve fitting or forward modeling, and the hybrid radar-radiometer algorithm does not require ancillary input data. The lack of forward modeling, curve fitting, or ancillary data requirements indeed differentiates this algorithm from many existing radar-based SSM retrieval techniques [6], [7], [8]. Accordingly, this study used the same change-detection-based approach to fuse data from the WindSat polarimetric radiometer and Advanced Microwave Scanning Radiometer 2 (AMSR2) sensor suites and the SMAP L-band radar (independent of the SMAP radiometer) to demonstrate that radar and radiometer observations need not be simultaneous in order for the algorithm to achieve accurate results. WindSat and AMSR2 were chosen to constrain the radar algorithm. Although WindSat and AMSR2 retrievals were somewhat less accurate than passive SMAP retrievals for the validation sites considered here, this study has shown that in most cases, WindSat or AMSR2 observations were still good enough to guide the radar retrieval algorithm.

The remainder of the article is organized as follows. Section II describes the hybrid radar-radiometer SSM retrieval algorithm.

Manuscript received 16 May 2022; revised 12 September 2022 and 18 October 2022; accepted 26 October 2022. Date of publication 3 November 2022; date of current version 14 November 2022. This work was supported in part by the Office of Naval Research (Funding Doc. No. N0001422WX00033) and in part by the U.S. Department of Agriculture, Agricultural Research Service. USDA is an equal opportunity provider and employer. A contribution to this work was made at the Jet Propulsion Laboratory, California Institute of Technology, under a contract with the National Aeronautics and Space Administration. (Corresponding author: Jeffrey D. Ouellette.)

Jeffrey D. Ouellette, Tanish Himani, Li Li, and Elizabeth M. Twarog are with the Naval Research Laboratory, Remote Sensing Division, Washington, DC 20375 USA (e-mail: jeffrey.ouellette@nrl.navy.mil; tanish.himani@nrl.navy.mil; li.li@nrl.navy.mil; elizabeth.twarog@nrl.navy.mil).

Andreas Colliander is with the NASA Jet Propulsion Laboratory, California Institute of Technology, Pasadena, CA 91109 USA (e-mail: andreas.colliander@jpl.nasa.gov).

David Goodrich and Chandra Holifield Collins are with the US Department of Agriculture, Agricultural Research Service, Southwest Watershed Research Center, Tucson, AZ 85719 USA (e-mail: dave.goodrich@usda.gov; Chandra.Holifield@usda.gov).

Michael Cosh is with the US Department of Agriculture, Agricultural Research Service, Beltsville, MD 20705 USA (e-mail: michael.cosh@usda.gov).

Jeffrey P. Walker is with the Department of Civil Engineering, Monash University, Clayton 3800, Australia (e-mail: jeff.walker@monash.edu).

Digital Object Identifier 10.1109/JSTARS.2022.3219259

Section III displays the error performance of the algorithm for four diverse validation sites, where retrieved SSM is compared with aggregates of in-situ probe measurements. Section IV presents the conclusions of this work.

II. ALGORITHM FORMULATION

This section describes the radar- and radiometer-based algorithm for SSM estimation. The radiometer algorithms remain independent of radar observations, and utilize the τ - ω approximation as a forward model to derive SSM from 1) the multifrequency, polarimetric WindSat radiometer suite [9], [10] and 2) dual-polarized, single frequency measurements (h and v at 6.9 GHz) from the AMSR2 radiometer suite. The radar portion of the algorithm was a time-series change detection approach whose solution space was locally bounded by radiometer-derived lower and upper limits for the SSM.

A. Radar SSM Retrieval Algorithm

The algorithm used in this study is applied to a time series of 3-km-resolution SMAP L-band radar backscatter observations, and is originally derived from the so-called ‘‘alpha approximation’’ [11]. The alpha approximation is based on the assumption that for a given observed scene, the ratio of consecutively measured, copolarized radar backscatter coefficients (measured at times t_1 and t_2) is equivalent to the squared ratio of corresponding alpha coefficients, such that

$$\frac{\sigma_{pp}^{0(t_2)}}{\sigma_{pp}^{0(t_1)}} \approx \left| \frac{\alpha_{pp}^{(t_2)}(\epsilon_s, \theta_i)}{\alpha_{pp}^{(t_1)}(\epsilon_s, \theta_i)} \right|^2 \quad (1)$$

where $\sigma_{pp}^{0(t_i)}$ is the pp -polarized radar backscatter coefficient (in linear units), and $\alpha_{pp}^{(t_i)}$ is the pp -polarized alpha coefficient for the observed scene at time t_i . The alpha coefficient is dependent on the soil permittivity ϵ_s and the incidence angle θ_i according to

$$\left| \alpha_{hh}^{(t_i)}(\epsilon_s^{(t_i)}, \theta_i) \right| = \left| \frac{(\epsilon_s^{(t_i)} - 1)}{(\cos \theta_i + \sqrt{\epsilon_s^{(t_i)} - \sin^2 \theta_i})^2} \right|$$

$$\left| \alpha_{vv}^{(t_i)}(\epsilon_s^{(t_i)}, \theta_i) \right| = \left| \frac{(\epsilon_s^{(t_i)} - 1)[\sin^2 \theta_i - \epsilon_s^{(t_i)}(1 + \sin^2 \theta_i)]}{(\epsilon_s^{(t_i)} \cos \theta_i + \sqrt{\epsilon_s^{(t_i)} - \sin^2 \theta_i})^2} \right|. \quad (2)$$

Note that for a fixed, known incidence angle, the soil permittivity can be directly inverted from (2). In turn, the SSM content for the observed scene can be derived from the soil permittivity via a dielectric mixing model (DMM). The DMM used in this study is the Peplinski–Ulaby–Dobson model [12]. Given a revisit time on the order of days, (1) approximates the surface roughness and vegetation biomass in the observed scene to be the same for times t_1 and t_2 , and further approximates the vegetation contribution as only a multiplicative contribution to the signal scattered from the soil surface [5]. In addition, soil surface roughness contribution is also assumed to be strictly multiplicative, as is the case in first-order analytical rough surface scattering theories such as the small perturbation method and the first-order small slope approximation [13]. Therefore, under the alpha approximation’s

assumptions, changes in consecutive radar backscatter measurements at a particular incidence angle for a particular scene can be entirely attributed to changes in SSM content. The hh - and vv -polarized radar backscatter coefficients can be organized into a matrix equation to solve for the unknown alpha coefficients at each element of the time series, such that

$$\begin{bmatrix} M_{hh} & M_0 \\ M_0 & M_{vv} \end{bmatrix} \begin{bmatrix} |\alpha_{hh}^{(t1)}| \\ |\alpha_{hh}^{(t2)}| \\ \vdots \\ |\alpha_{hh}^{(tN)}| \\ |\alpha_{vv}^{(t1)}| \\ |\alpha_{vv}^{(t2)}| \\ \vdots \\ |\alpha_{vv}^{(tN)}| \end{bmatrix} = \begin{bmatrix} 0 \\ 0 \\ \vdots \\ 0 \\ 0 \\ 0 \\ \vdots \\ 0 \end{bmatrix} \quad (3)$$

where M_0 is the zero matrix, N is the number of radar observations in the time series, and

$$M_{pp} = \begin{bmatrix} 1 & -\sqrt{\frac{\sigma_{pp}^{0(t1)}}{\sigma_{pp}^{0(t2)}}} & 0 & \dots & 0 & 0 \\ 0 & 1 & -\sqrt{\frac{\sigma_{pp}^{0(t2)}}{\sigma_{pp}^{0(t3)}}} & \dots & 0 & 0 \\ \vdots & \ddots & \ddots & \ddots & \ddots & \vdots \\ 0 & 0 & 0 & \dots & 1 & -\sqrt{\frac{\sigma_{pp}^{0(N-1)}}{\sigma_{pp}^{0(N)}}} \end{bmatrix}. \quad (4)$$

Note that the matrix in (3) is a rectangular, $2(N-1) \times 2N$ matrix, i.e., the matrix equation is underdetermined. A bounded linear least squares regression was therefore applied to solve (3). Previous studies have shown that the alpha approximation algorithm performs poorly when bounded only by extremely dry and extremely wet soil conditions ($0.03 \text{ m}^3/\text{m}^3$ and $0.45 \text{ m}^3/\text{m}^3$, respectively) [5], [11]. Hard bounds for this linear least squares optimization were thus derived from coarser resolution (25 km) WindSat/AMSR2 SSM data products. Solving (4) via bounded linear least squares required the conversion of these minimum and maximum SSM bounds into alpha coefficient bounds. This conversion was performed by first inverting the Peplinski–Ulaby–Dobson DMM (with ancillary soil texture information) to derive relative soil permittivities from SSM values, then using those permittivities to derive alpha coefficients via (2).

B. Radiometer SSM Retrieval Algorithms

The WindSat and AMSR2 SSM retrieval algorithms have each been used to derive local minimum and maximum bounds for SSM over the 84-day time series containing observations of SMAP L-band radar data. SMAP and WindSat sensor data have been collected from a polar orbit with an average revisit time of three days for the study regions considered here, but these observations seldom share a temporal overlap with each other. For AMSR2’s polar orbit, the average revisit time was two days. The discrepancy between radiometer and radar spatial

resolutions was resolved by using the radiometer pixel whose center point was closest to that of the radar pixel.

WindSat's land surface algorithm simultaneously retrieves SSM, vegetation water content, and land surface temperature (T_s) by comparing multichannel radiometer brightness temperature with a forward model. The AMSR2 algorithm works similarly, but uses a dual-polarized, single-frequency algorithm for each radiometer frequency band to simultaneously derive SSM and vegetation optical depth. The authors have chosen to use the lower C-band (6.9 GHz) channel due to its theoretical capacity to better penetrate foliage. The forward model used for both sensors was the τ - ω approximation, which assumes the surface brightness temperature for p -polarization T'_{Bp} (unmodified by atmospheric attenuation or scattering) is given by

$$T'_{Bp} = T_s e_{sp} \exp(-\tau_c) + T_s (1 - \omega_p) (1 - \exp(-\tau_c)) [1 + r_{sp} \exp(-\tau_c)] \quad (5)$$

where e_{sp} and $r_{sp} = 1 - e_{sp}$ are respectively the soil emissivity and soil reflectivity, ω_p is an empirically derived parameter accounting for scattering and emission from vegetation, and τ_c is the slant optical depth of the vegetation canopy. The measured brightness temperature T_{Bp} is a modification of T'_{Bp} , which accounts for atmospheric effects, such that

$$T_{Bp} = T_{Bu} + \exp(-\tau_a)(T'_{Bp} + r_{sp}T_{Bd}) \quad (6)$$

where T_{Bu} and T_{Bd} are the upwelling and downwelling atmospheric emission and τ_a is the slant atmospheric opacity. The WindSat SSM algorithm uses linear polarimetric data from WindSat's 10.7, 18.7, and 37 GHz channels [9], [10] while the AMSR2 algorithm uses dual-polarized (h and v) data at 6.9 GHz [14].

III. RESULTS AND DISCUSSION

Figs. 1 and 2 show the algorithm performance at a representative 3 km reference pixel for each validation site used in this study, with Fig. 1 corresponding to the WindSat-bounded algorithm and Fig. 2 showing results using AMSR2. The four validation sites, in order of their appearance in Figs. 1 and 2, are respectively located in Yanco, New South Wales, Australia [15], Walnut Gulch, Arizona, USA [16], Kenaston, Manitoba, Canada [17], and Fredricksburg, Texas, USA [18]. These validation sites were chosen for their high densities of hydraprobes, making comparisons with 3 km SSM products feasible and meaningful. Measurements for individual in-situ dielectric hydraprobes (represented by the thin, dotted-and-dashed curves in Figs. 1 and 2) were linearly averaged to form a composite in-situ measurement for each 3 km pixel at each validation site (represented by the bold, solid green curves in Figs. 1 and 2). This 3 km average provided the baseline against which the retrieval algorithm's SSM estimates (represented by the dark blue circles in Figs. 1 and 2) were assessed.

The results in Fig. 1 suggest the SMAP-WindSat retrieval algorithm was qualitatively and quantitatively effective over a broad range of observation conditions. Qualitatively, the retrieval algorithm appeared to effectively track day-to-day changes in SSM for each of the validation site reference pixels

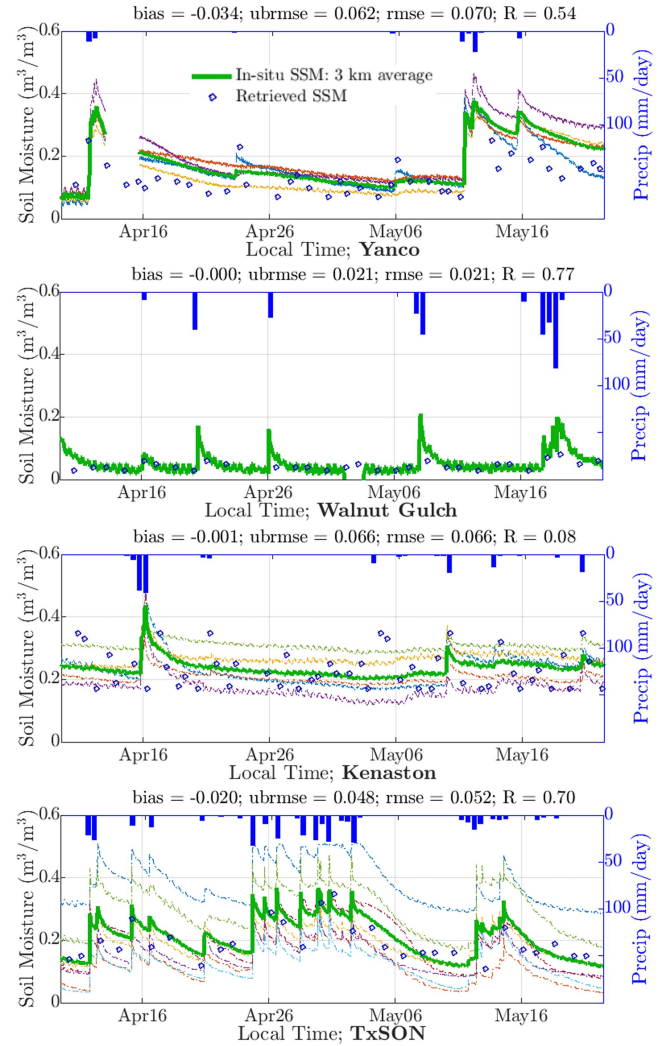


Fig. 1. Time-series data for a representative 3 km reference pixel within each of the four validation sites. Data for individual in-situ measurement hydraprobes are shown as thin, dotted-and-dashed lines in each plot. The linear average of probe measurements for each reference pixel is represented by the solid, dark green curves. SSM retrievals using the SMAP radar and WindSat radiometer are plotted as blue circles. The error bias (m^3/m^3), unbiased RMSE (m^3/m^3), RMSE (m^3/m^3), and R -value are reported at the top of each plot. Refer to Fig. 4 (top) for information on the constraints derived from WindSat and applied to the SMAP radar data.

in Fig. 1. The magnitude of the algorithm's bias for volumetric estimates was below $0.04 \text{ m}^3/\text{m}^3$ in each case. For each reference pixel, the RMSE ranges between $0.022 \text{ m}^3/\text{m}^3$ to $0.066 \text{ m}^3/\text{m}^3$ and the R -value (a measure of the correlation between retrieved and measured SSM) is above 0.5 for every pixel except the one in Kenaston. Fig. 2, which showcases results from the SMAP-AMSR2 algorithm, displays similar performance to the SMAP-WindSat case, but slightly worse results for the Kenaston site. This could be because the AMSR2 algorithm is a single-frequency-channel algorithm whose vegetation optical depth measurements are less reliable than those from a multi-frequency-channel algorithm.

For both WindSat- and AMSR-2-derived constraints, the algorithm performance at the Kenaston site was noticeably worse than for the other validation sites, partly due to a number of precipitation events which were not captured by the hydraprobes

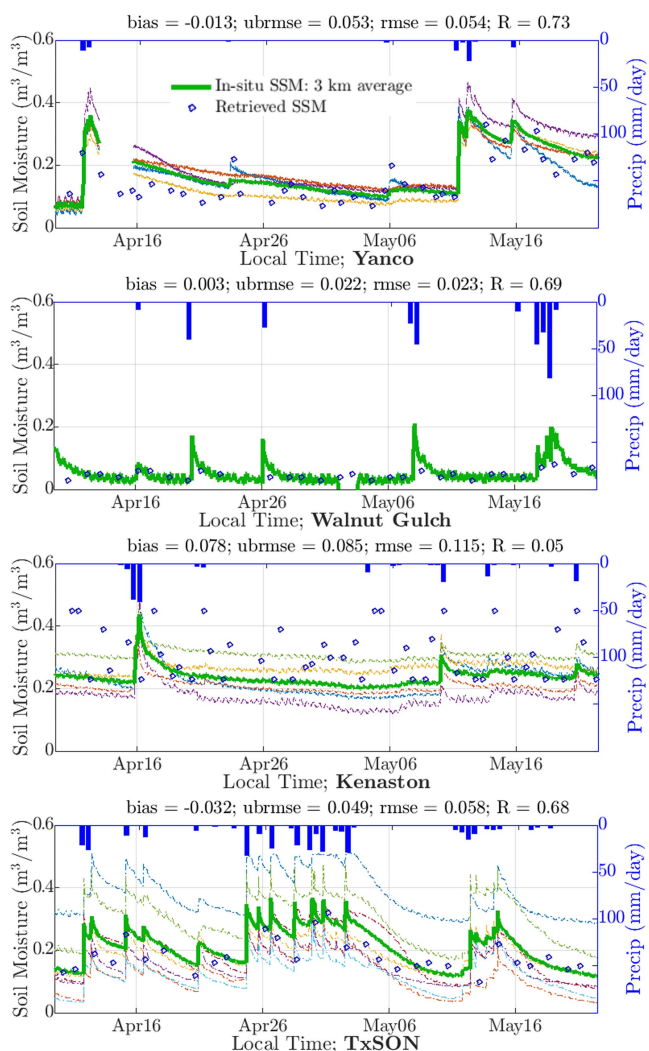


Fig. 2. Same as Fig. 1, except the retrievals use the SMAP radar and AMSR2 radiometer, which are plotted as blue circles. The linear average of probe measurements for each reference pixel is represented by the solid, dark green curves. Data for individual in-situ measurement hydraprobes are shown as thin, dotted-and-dashed lines. The error bias (m^3/m^3), unbiased RMSE (m^3/m^3), RMSE (m^3/m^3), and R -value are reported at the top of each plot. Refer to Fig. 4 (bottom) for information on the constraints derived from AMSR2 and applied to the SMAP radar data.

due to their soil depth. Further discrepancies can be explained by the heterogeneity of the agricultural landscape and its effect on the orbit-to-orbit radar backscatter signal [17], [19]. Each of the instruments observed in this study was conically scanned, and strong scan-to-scan and/or orbit-to-orbit fluctuations due to heterogeneity would certainly introduce significant errors into a change-detection-based retrieval algorithm. The algorithm was shown to display less significant errors from airborne, side-looking SAR measurements taken in a similar environment during the SMAPVEX12 experimental field campaign [5].

Fig. 3 shows the overall error performance for each validation site, computed over all 3 km reference pixels at each site. The RMSE for each site was reported within the figure. The overall RMSE for the SMAP-WindSat retrieval

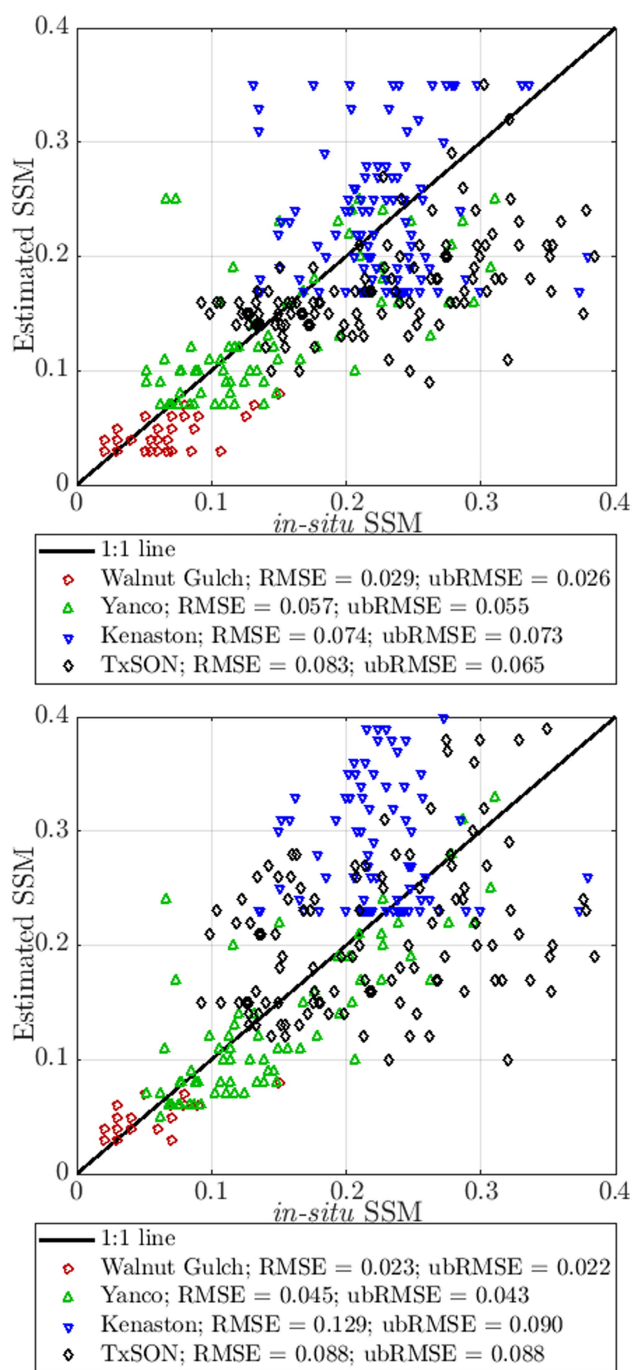


Fig. 3. Active/passive retrieved SSM versus in-situ measurements (3 km average) for every 3 km reference pixel within every validation site. RMSE and unbiased RMSE are reported for each site, across all its reference pixels. Top: SMAP/WindSat; bottom: SMAP/AMSR2.

algorithm, taken across all reference pixels considered in the study, was $0.070 m^3/m^3$, while the unbiased RMSE was $0.067 m^3/m^3$. For the SMAP-AMSR2 algorithm, the overall RMSE was $0.093 m^3/m^3$ and the unbiased RMSE was $0.090 m^3/m^3$. Examining Fig. 3, the larger RMSE for the SMAP-AMSR2 case seems to be driven by the relatively poor performance of the algorithm at the Kenaston site. The Kenaston site shows poorer error performance compared with the remaining

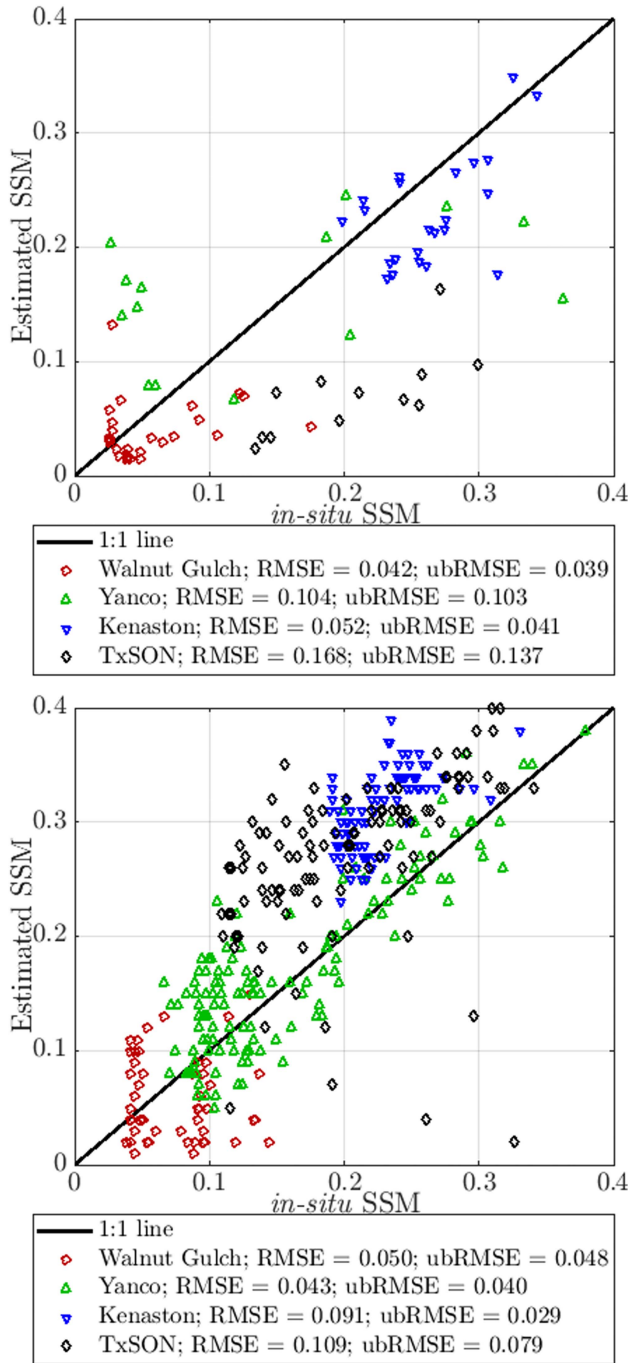


Fig. 4. Passive retrieved SSM versus in-situ measurements (25 km average) for every 25 km reference pixel within every validation site. RMSE and unbiased RMSE are reported for each site, across all its reference pixels. Top: WindSat; bottom: AMSR2. Note there are many more AMSR2 measurements than WindSat measurements due to AMSR2 having a slightly higher revisit time and fewer quality control flags.

validation sites for the aforementioned reasons, with the algorithm tending toward the lower and upper limits derived from both WindSat and AMSR2 radiometer estimates.

For reference, the 25-km passive WindSat SSM retrievals are shown as a function of 25 km in-situ probe averages in Fig. 4 (top). Passive AMSR2 retrievals versus ground truth are shown in Fig. 4 (bottom). Note that the TxSON and Yanco sites have

proven especially problematic for the WindSat retrievals. Since 10.7 GHz was the lowest radiometer frequency channel used for the WindSat soil moisture product, topographic effects, and vegetation in these areas likely obscured upwelling radiation from the underlying soil surface. L-band microwave frequencies are less sensitive to these conditions, hence the higher sensitivity of SMAP active and passive observations to changes in SSM. AMSR2 tends to overestimate soil moisture in both the TxSON and Kenaston study regions, likely due to issues arising from estimating vegetation optical depth using a single-frequency algorithm. Despite their shortcomings in the study regions, WindSat and AMSR2 observations seem generally sufficient to guide the alpha approximation retrieval algorithm toward a fairly accurate solution.

IV. CONCLUSION

This article has presented an error analysis of an SSM retrieval algorithm that was designed to receive input data in the form of a time series of polarimetric radar backscatter and radiometer brightness temperature observations. In this study, the algorithm used input data from the SMAP L-band synthetic aperture radar and derived constraints from either the WindSat multifrequency polarimetric radiometer suite or the AMSR2 C-band (6.9 GHz) radiometer channel. The algorithm uses a time series of ratios between consecutive radar backscatter measurements, cast as a matrix equation and constrained by radiometer-derived lower and upper limits to the retrieved SSM. The radiometer retrieval algorithms, which were used to derive these constraints, both utilized a zeroth-order approximation to the radiative transfer equation commonly known as the τ - ω model. The hybrid radar-radiometer retrieval algorithm's performance was assessed against four soil moisture validation sites, consisting of dense in-situ networks of hydra probes. SMAP-WindSat algorithm error performance exhibited an RMSE of $0.070 \text{ m}^3/\text{m}^3$ and an unbiased RMSE of $0.067 \text{ m}^3/\text{m}^3$ across all validation sites. SMAP-AMSR2 algorithm error performance was found to exhibit an RMSE of $0.093 \text{ m}^3/\text{m}^3$ and an unbiased RMSE of $0.090 \text{ m}^3/\text{m}^3$ across all validation sites. The SMAP-WindSat algorithm error performance is comparable to the SMAP active baseline algorithm in both RMSE and unbiased RMSE [19], though SMAP-AMSR2 is somewhat worse. The methodology described herein achieved reasonable results without the aid of ancillary information or the need for training data, and furthermore demonstrated synergy between disparate and nonsimultaneous microwave remote sensing observations.

ACKNOWLEDGMENT

This research was a contribution from the USDA Long-Term Agroecosystem Research (LTAR) network. The authors would furthermore like to extend their thanks to the researchers at the USDA, the University of Guelph, the University of Texas at Austin, and Monash University, for making the in-situ soil moisture data available for use.

REFERENCES

- [1] T. Schmugge, P. Gloersen, T. Wilheit, and F. Geiger, "Remote sensing of soil moisture with microwave radiometers," *J. Geophys. Res.*, vol. 79, no. 2, pp. 317–323, 1974.
- [2] R. Newton and J. Rouse, "Microwave radiometer measurements of soil moisture content," *IEEE Trans. Antennas Propag.*, vol. 28, no. 5, pp. 680–686, Sep. 1980.
- [3] F. T. Ulaby, R. K. Moore, and A. K. Fung, *Microwave Remote Sensing: Active and Passive*, vol. 2. Norwood, MA, USA: Artech House, 1986.
- [4] X. Zhan, P. R. Houser, J. P. Walker, and W. T. Crow, "A method for retrieving high-resolution surface soil moisture from HYDROS 1-band radiometer and radar observations," *IEEE Trans. Geosci. Remote Sens.*, vol. 44, no. 6, pp. 1534–1544, Jun. 2006.
- [5] J. D. Ouellette et al., "A time-series approach to estimating soil moisture from vegetated surfaces using 1-band radar backscatter," *IEEE Trans. Geosci. Remote Sens.*, vol. 55, no. 6, pp. 3186–3193, Jun. 2017.
- [6] W. Wagner and K. Scipal, "Large-scale soil moisture mapping in western africa using the ERS scatterometer," *IEEE Trans. Geosci. Remote Sens.*, vol. 38, no. 4, pp. 1777–1782, Jul. 2000.
- [7] Y. Kim and J. J. van Zyl, "A time-series approach to estimate soil moisture using polarimetric radar data," *IEEE Trans. Geosci. Remote Sens.*, vol. 47, no. 8, pp. 2519–2527, Aug. 2009.
- [8] S.-B. Kim et al., "SMAP algorithm theoretical basis document: L2 & L3 radar soil moisture (active) products," Jet Propuls. Lab., Pasadena, CA, USA, Tech. Rep. JPL D-66479, 2014.
- [9] L. Li, P. W. Gaiser, T. J. Jackson, R. Bindlish, and J. Du, "WindSat soil moisture algorithm and validation," in *Proc. IEEE Int. Geosci. Remote. Sens. Symp.*, 2007, pp. 1188–1191.
- [10] L. Li et al., "WindSat global soil moisture retrieval and validation," *IEEE Trans. Geosci. Remote Sens.*, vol. 48, no. 5, pp. 2224–2240, May 2010.
- [11] A. Balenzano, F. Mattia, G. Satalino, and M. W. J. Davidson, "Dense temporal series of C- and L-band SAR data for soil moisture retrieval over agricultural crops," *IEEE J. Sel. Topics Appl. Earth Observ. Remote Sens.*, vol. 4, no. 2, pp. 439–450, Jun. 2011.
- [12] N. R. Peplinski, F. T. Ulaby, and M. C. Dobson, "Dielectric properties of soils in the 0.3–1.3-GHz range," *IEEE Trans. Geosci. Remote Sens.*, vol. 33, no. 3, pp. 803–807, May 1995.
- [13] A. G. Voronovich, *Wave Scattering From Rough Surfaces*, vol. 2. Berlin, Germany: Springer, 1994.
- [14] J. Liu and X. Zhan, "Algorithm theoretical basis document: GCOM-W1/AMSR2 soil moisture product," NOAA, Washington, DC, USA, Tech. Rep., 2016.
- [15] R. Panciera et al., "The soil moisture active passive experiments (SMAPEX): Toward soil moisture retrieval from the SMAP mission," *IEEE Trans. Geosci. Remote Sens.*, vol. 52, no. 1, pp. 490–507, Jan. 2014.
- [16] D. C. Goodrich et al., "Runoff simulation sensitivity to remotely sensed initial soil water content," *Water Resour. Res.*, vol. 30, no. 5, pp. 1393–1405, 1994.
- [17] E. Tetlock et al., "An 11-year (2007–2017) soil moisture and precipitation dataset from the Kenaston Network in the Brightwater Creek basin, Saskatchewan, Canada," *Earth Syst. Sci. Data*, vol. 11, no. 2, pp. 787–796, 2019.
- [18] T. G. Caldwell et al., "The Texas soil observation network: A comprehensive soil moisture dataset for remote sensing and land surface model validation," *Vadose Zone J.*, vol. 18, no. 1, pp. 1–20, 2019.
- [19] A. Colliander et al., "Validation of SMAP surface soil moisture products with core validation sites," *Remote Sens. Environ.*, vol. 191, pp. 215–231, 2017.